



# A multi-city epidemiological model based on cellular automata and complex networks for the COVID-19

Cássio de Lima Quiroga<sup>1</sup> · Pedro Henrique Triguís Schimit<sup>1</sup>

Received: 24 May 2022 / Revised: 17 June 2023 / Accepted: 11 July 2023 /  
Published online: 21 August 2023

© The Author(s) under exclusive licence to Sociedade Brasileira de Matemática Aplicada e Computacional 2023

## Abstract

Multi-patch and multi-city models have been proposed to investigate the dynamics of disease propagation in discrete regions characterized by varying connectivity and movement rates. This paper aims to comprehensively explore the impact of network topology and travel rates on disease spread within a population represented by random networks of interconnected cities. This approach enables a more comprehensive analysis of disease outbreaks across spatial domains compared to conventional multi-patch models, which typically consider a limited number of homogeneous links among subpopulations within distinct spatial units (i.e., patches). In this study, cities are represented using a probabilistic cellular automaton model that incorporates local interactions among individuals, while the network's edges represent the travel rates between pairs of cities (i.e., nodes). Two types of complex networks are considered, namely small-world and Barabási–Albert networks. By employing a flexible numerical model, this study surpasses previous models in its capacity to accommodate a larger number of patches or cities. The primary findings of this research reveal that reducing the travel rates within the network can potentially “flatten the curve” of infected cases; however, it does not impact the population's basic reproduction number. To effectively reduce the reproduction number, localized interventions targeting disease transmissibility are required. Additionally, concentrating control efforts on “central” cities within the network may prove crucial in impeding the rapid propagation of the disease. In summary, this study employs a rigorous framework to investigate the influence of network topology and travel rates on disease spreading within a population represented by random networks of interconnected cities. The findings contribute to a comprehensive understanding of disease dynamics in complex spatial settings and inform targeted intervention strategies for controlling and mitigating infectious disease outbreaks.

---

Communicated by Rafael Villanueva.

✉ Pedro Henrique Triguís Schimit  
schimit@alumni.usp.br; schimit@uni9.pro.br

Cássio de Lima Quiroga  
cassio.de@uni9.edu.br

<sup>1</sup> Informatics and Knowledge Management Graduate Program, Universidade Nove de Julho, Rua Vergueiro, 235/249, São Paulo, SP 01525-000, Brazil

**Keywords** Disease spreading · Multi-city network · Patch models · Probabilistic cellular automata · SIR model

**Mathematics Subject Classification** 92D25 · 92D30

## 1 Introduction

One of the fundamental assumptions in mathematical modeling of epidemiological dynamics involves the utilization of large populations, where individuals are uniformly distributed in space, and there is homogeneous mixing among individuals in different stages of the disease (Anderson and May 1991; Kermack and McKendrick 1927; Rock et al. 2014). Initially, these models were formulated based on differential equations. However, as research progressed, Cellular Automata (CA) emerged as an alternative approach to capture spatial characteristics of the host and heterogeneous populations (Ahmed et al. 1998; Johansen 1996; Sirakoulis et al. 2000; Yakowitz et al. 1990; Wolfram 1994). These studies explored variations of the classical SIR model (Susceptible–Infected–Removed) (Anderson and May 1991) within the context of cellular automata frameworks.

Cellular Automata have been extensively employed to investigate various aspects of epidemiological dynamics. Different neighborhood configurations have been considered to facilitate local interactions among individuals, as demonstrated in previous studies Ahmed et al. (1998), Sirakoulis et al. (2000), Yakowitz et al. (1990), Ramos and Schimit (2019) and Monteiro et al. (2020). Moreover, researchers have explored the incorporation of long-range connections into cellular automata models (Ogren and Martin 2000; Schimit and Monteiro 2009), as well as the integration of global components (Cissé et al. 2016). Furthermore, the heterogeneity of population dispersion in a landscape has been addressed through diverse approaches. Some studies have explored the variation in individuals' density per cell in cellular automata models (Medrek and Pastuszak 2021). Others have focused on the use of multi-agent systems concentrated in specific areas interconnected through complex networks (GwizdaHa 2020) or demographic structures (Castellazzo et al. 2012). Complex networks have also been utilized to replicate population dynamics, employing classical network models such as small world (Moore and Newman 2000) and scale free (Colizza et al. 2007), as well as networks with complex connection structures (Franc 2004; Sander et al. 2002). Additionally, complex networks have proven valuable in the analysis of spatial patterns of disease propagation (Dorjee et al. 2013; Rautureau et al. 2010; Schimit and Pereira 2018; van Ravensway et al. 2012; Westgarth et al. 2009).

Another approach to model the heterogeneous spatial distribution of individuals involves the concept of multi-patches (Salmani 2006; Wang and Zhao 2006) or multi-cities (Arino and Van Den Driessche 2003). In these studies, the population is dispersed among discrete patches or cities, with local interactions occurring within each patch and movement rates between patches. While some analytical studies have considered a large number of patches, the corresponding numerical results typically involve a limited number of patches. For instance, previous works have utilized two (Wang and Zhao 2006; Kheiri and Jafari 2019; Kouokam et al. 2008; Liu et al. 2018; Prosper et al. 2012; Wang and Zhao 2008), five (Senapati et al. 2019), nine (Allen et al. 2007; Zakary et al. 2017), and fifteen (Arino et al. 2007) patches. Variations of the SIR model have been employed to examine diseases such as HIV/AIDS (Kheiri and Jafari 2019), tuberculosis (Kheiri and Jafari 2019), and dengue (Senapati et al. 2019) in these multi-patch frameworks.

Splitting individuals into distinct patches introduces heterogeneity in population dispersion across space. Instead of considering a single large homogeneous population, multi-patch models involve the division of the population into large, homogeneous subpopulations that are spatially separated. The interplay between these subpopulations is characterized by the movement or travel rate of individuals. This modeling approach aims to investigate the spread of diseases within the system, taking into account the connections among patches, and to propose control measures for managing outbreaks. Examples of such control measures include travel-blocking (Zakary et al. 2016), optimal control strategies for travel-blocking (Zakary et al. 2017), mosquito control strategies to study dengue prevalence within patches (Senapati et al. 2019), and the distribution of vaccinations across patches (Cui et al. 2017). Notably, the COVID-19 pandemic has also been studied within a multi-patch framework, examining regions such as the Hubei province and areas outside of it (Chandrasekaran and Fernandes 2020).

Although some models have taken into account an asymmetric connectivity matrix for the network of patches (Chen et al. 2020; Mpolya et al. 2014), the majority of studies have focused on regular networks with uniform connections between patches. These connections range from sparse links among patches (Senapati et al. 2019) to star networks, where one city is connected to all others (Allen et al. 2007; Zakary et al. 2017; Mpolya et al. 2014). Consequently, the objective of this paper is to examine cities and their connections as random networks to investigate the influence of network topology and travel rates on disease propagation throughout the entire population. To achieve this, numerical simulations are conducted to encompass a diverse range of undirected network types and population mobility patterns within and between cities. Subsequently, we adopt the term “city” as a unifying nomenclature to represent discrete geographical regions in which a fraction of the overall population resides.

The movement of individuals between cities within a region is driven by various factors, including services, health facilities, employment, and housing (Aranha 2005; Fiocruz 2020). However, quantifying the specific impact of each category on the spread of diseases such as COVID-19 has proven challenging. During the COVID-19 pandemic, researchers conducted statistical analyses comparing pre-pandemic patterns of intercity mobility to the period when border lockdown measures were implemented, aiming to assess the resulting reduction in COVID-19 transmission (Chinazzi et al. 2020). The technical reports published by the Oswaldo Cruz Foundation (Fiocruz) shed light on the influence of intercity flows on the dynamics of COVID-19 transmission in Brazilian cities, taking into account factors such as hospital access and vaccine distribution (Notas 2022). Consequently, the utilization of multi-city models based on random network theory enables the emulation of various categories of individual mobility, facilitating the derivation of general conclusions irrespective of specific network topologies.

In this study, we adopt a probabilistic cellular automaton (PCA) framework to model individual behavior within a city, with each cell representing an individual in one of the SAIR model states (Susceptible, infected Asymptomatic, infected Symptomatic, Recovered), similar to Monteiro (2020). By considering cities as nodes and the connections between them as edges in a network, we simulate the spread of disease throughout the population. Specifically, we assume an initial outbreak in one of the cities, and the rate at which individuals travel between connected cities determines the transmission of the disease across the network.

Using this framework, we conduct simulations to gain insights into the dynamics of disease outbreaks and explore strategies for outbreak control across various network topologies. To assess the characteristics of the networks, we examine several parameters, including average shortest path, density, diameter, clustering coefficient, average degree, and maximum

degree. Among these measures, the clustering coefficient emerges as particularly informative, as it quantifies the fraction of connections among neighbors of the same node, averaged over the entire network. Moreover, we employ additional metrics such as degree centrality, closeness centrality, and betweenness centrality to identify central cities within the network and compare the effectiveness of disease control actions.

By employing a flexible numerical model, the scope of patch consideration surpasses that of conventional models discussed earlier. By augmenting the number of patches, the model effectively captures the intricate interplay of various factors and interactions among neighboring regions, thereby providing a more authentic representation of disease spread. Furthermore, an increased number of patches allows for a more meticulous examination of the impact of spatial heterogeneity on disease transmission. In this context, the spatial heterogeneity of population distribution is modeled through the network of patches.

Lastly, a higher number of patches facilitate a comprehensive evaluation of intervention strategies. With an expanded patch count, it is possible to explore the effectiveness of interventions aimed at specific regions, evaluate the repercussions of travel restrictions, and investigate the role of vaccination campaigns across multiple patches (Klepac et al. 2016; Zhao et al. 2018). This provides valuable insights into optimizing interventions at both local and global levels to control and mitigate the spread of infectious diseases.

This paper is structured as follows. Section 2 provides a detailed description of the proposed model, including its key components and underlying assumptions. The simulation results are presented in Sect. 3, where the numerical outcomes of the model under various scenarios are analyzed and interpreted. In Sect. 4, a discussion is presented.

## 2 Methods

### 2.1 The PCA model

One city is represented by a cellular automaton structured as an  $n \times n$  lattice with  $N$  cells, where each cell accommodates a single individual. To avoid edge effects, the borders of the lattice are connected, such that the top row is linked to the bottom row and the first column is connected to the last column. The neighborhood of a given cell encompasses  $C$  randomly selected cells within this a  $r$  Moore radius (Wolfram 1994). The probability of having a neighbor from a specific layer  $i$  (defined by the Chebyshev distance  $i$ ) is calculated using the expression  $q_{i,r} = 2(r+1-i)/r(r+1)$  (Schimit and Monteiro 2009). For instance, considering a Moore radius of 4, the probabilities of having a neighbor from layers 1, 2, 3, and 4 are, respectively, given by  $q_{1,4} = 0.4$ ,  $q_{2,4} = 0.3$ ,  $q_{3,4} = 0.2$ , and  $q_{4,4} = 0.1$ . Subsequently, after randomly selecting the layer, one cell from the chosen layer is considered as the neighbor (Schimit and Monteiro 2009).

In this lattice, individuals are classified into four distinct states based on their COVID-19 status: Susceptible ( $S$ ), Asymptomatic Infected ( $I_A$ ), Symptomatic Infected ( $I_S$ ), and Recovered ( $R$ ). The state transitions are as follows: susceptible individuals can be infected with a probability denoted by  $P_I(v) = 1 - e^{-kv}$ , where  $v$  represents the total number of infected neighbors ( $I_A + I_S$ ), and  $k$  is a parameter associated with the disease's infectivity. Asymptomatic (symptomatic) infected individuals can either recover with a probability denoted by  $P_{C_A}$  ( $P_{C_S}$ ) and transition to the recovered state, or they may succumb to the disease with a probability denoted by  $P_{D_A}$  ( $P_{D_S}$ ). Recovered individuals may also experience mortality due to other causes, characterized by a probability denoted by  $P_N$ . To maintain a constant

population size, susceptible individuals replace those who have died. Consequently, each time-step of the simulation consists of establishing  $C$  connections per individual, evaluating the state transitions based on the respective probabilities, and synchronously updating the states at the end of the time-step. The total number of time-steps in a simulation is denoted as  $t_s$ .

The next step is to describe the model in terms of ordinary differential equations (ODE).

### 2.2 The ODE model

The state transitions can be interpreted as rates. When considering a large population where individuals in susceptible, both infected, and recovered states are uniformly distributed across the lattice, an Ordinary Differential Equations (ODE) model can be employed to provide a mean-field approximation for the Probabilistic Cellular Automata (PCA) simulation of a single city:

$$\begin{aligned}
 \frac{dS(t)}{dt} &= -a_A S(t)[I_A(t) + I_S(t)] - a_S S(t)[I_A(t) + I_S(t)] + c_A I_A(t) + c_S I_S(t) + eR(t), \\
 \frac{dI_A(t)}{dt} &= a_A S(t)[I_A(t) + I_S(t)] - b_A I_A(t) - c_A I_A(t), \\
 \frac{dI_S(t)}{dt} &= a_S S(t)[I_A(t) + I_S(t)] - b_S I_S(t) - c_S I_S(t), \\
 \frac{dR(t)}{dt} &= b_A I_A(t) + b_S I_S(t) - eR(t),
 \end{aligned}
 \tag{1}$$

where  $a_A$  represents the infection rate constant that generates asymptomatic individuals,  $a_S$  denotes the infection rate constant responsible for generating symptomatic individuals,  $b_A$  signifies the recovering rate constant of asymptomatic individuals,  $b_S$  represents the recovering rate constant of symptomatic individuals,  $c_A$  indicates the death rate constant due to the disease for asymptomatic individuals,  $c_S$  represents the death rate constant resulting from the disease for symptomatic individuals, and  $e$  denotes the death rate constant due to other causes.

In line with the PCA model, the total population size remains constant, as indicated by the equation  $dS(t)/dt + dI_A(t)/dt + dI_S(t)/dt + dR_i(t)/dt = 0$ . Consequently, it holds that  $S(t) + I_A(t) + I_S(t) + R(t) = N$ . Furthermore, the parameters  $a_A, a_S, b_A, b_S, c_A, c_S,$  and  $e$  can be estimated through simulations, given that the ODE model serves as a mean-field approximation. The interconnections between these models, as outlined in Schimit and Monteiro (2009), are expressed as follows:

$$\begin{aligned}
 a_A &\simeq \frac{\Delta I_A(t)_{S \rightarrow I_A}}{S(t)(I_A(t) + I_S(t))\Delta t}, \\
 a_S &\simeq \frac{\Delta I_A(t)_{S \rightarrow I_S}}{S(t)(I_A(t) + I_S(t))\Delta t}, \\
 b_A &\simeq \frac{\Delta R(t)_{I_A \rightarrow R}}{I_A(t)\Delta t}, \\
 b_S &\simeq \frac{\Delta R(t)_{I_S \rightarrow R}}{I_A(t)\Delta t}, \\
 c_A &\simeq \frac{\Delta S(t)_{I_A \rightarrow S}}{I_i(t)\Delta t},
 \end{aligned}$$

$$\begin{aligned}
 c_S &\simeq \frac{\Delta S(t)_{I_S \rightarrow S}}{I_i(t)\Delta t}, \\
 e &\simeq \frac{\Delta S(t)_{R \rightarrow S}}{R(t)\Delta t},
 \end{aligned}
 \tag{2}$$

where  $\Delta I_A(t)S \rightarrow I_A$  represents the increase in asymptomatic infections  $I_A(t)$  due to new cases per time-step,  $\Delta I_S(t)S \rightarrow I_S$  represents the increase in symptomatic infections  $I_S(t)$  due to new cases per time-step,  $\Delta R(t)I_A \rightarrow R$  represents the increase in recoveries  $R(t)$  from asymptomatic infections per time step,  $\Delta R(t)I_S \rightarrow R$  represents the increase in recoveries  $R(t)$  from symptomatic infections per time-step,  $\Delta S(t)I_A \rightarrow S$  represents the increase in susceptible population  $S(t)$  due to deaths caused by asymptomatic infections,  $\Delta S(t)I_S \rightarrow S$  represents the increase in susceptible population  $S(t)$  due to deaths caused by symptomatic infections, and  $\Delta S(t)_{R \rightarrow S}$  represents the increase in susceptible population  $S(t)$  due to deaths from other causes per time-step. Therefore, each city is modeled independently using PCA and ODE.

An equilibrium point in the state space  $S \times I_A \times I_S \times R$  corresponds to a stationary solution that satisfies the following conditions:  $dS(t)/dt = 0$ ,  $dI_A(t)/dt = 0$ ,  $dI_S(t)/dt = 0$ , and  $dR(t)/dt = 0$ . Of particular interest is the disease-free equilibrium (DFE) denoted as  $(S, I_A, I_S, R) = (1, 0, 0, 0)$ . The DFE is commonly used to calculate the basic reproduction number ( $R_0$ ) using the next generation matrix method proposed by Van Den Driessche and Watmough (2002). In the context of considering  $\Phi$  cities, the basic reproduction number can be determined using the method presented in Arino and Van Den Driessche (2003). Since we are analyzing the system in a permanent regime to calculate  $R_0$ , where all cities are in an equilibrium state, we can disregard the individuals' travel rates among cities. By examining the equations given in Eq. 1, the infectious subsystem for all cities, with the exponent denoting the city number, can be expressed as follows:

$$\left\{ \begin{aligned}
 \frac{dI_A^1(t)}{dt} &= a_A^1 S^1(t)[I_A^1(t) + I_S^1(t)] - b_A^1 I_A^1(t) - c_A^1 I_A^1(t) \\
 \frac{dI_S^1(t)}{dt} &= a_S^1 S^1(t)[I_A^1(t) + I_S^1(t)] - b_S^1 I_S^1(t) - c_S^1 I_S^1(t) \\
 \frac{dI_A^2(t)}{dt} &= a_A^2 S^2(t)[I_A^2(t) + I_S^2(t)] - b_A^2 I_A^2(t) - c_A^2 I_A^2(t) \\
 \frac{dI_S^2(t)}{dt} &= a_S^2 S^2(t)[I_A^2(t) + I_S^2(t)] - b_S^2 I_S^2(t) - c_S^2 I_S^2(t) \\
 &\vdots \\
 \frac{dI_A^\Phi(t)}{dt} &= a_A^\Phi S^\Phi(t)[I_A^\Phi(t) + I_S^\Phi(t)] - b_A^\Phi I_A^\Phi(t) - c_A^\Phi I_A^\Phi(t) \\
 \frac{dI_S^\Phi(t)}{dt} &= a_S^\Phi S^\Phi(t)[I_A^\Phi(t) + I_S^\Phi(t)] - b_S^\Phi I_S^\Phi(t) - c_S^\Phi I_S^\Phi(t).
 \end{aligned} \right.
 \tag{3}$$

For this subsystem, the Jacobian matrix in the disease-free equilibrium  $((S^*, I_A^*, I_S^*, R^*) = (1, 0, 0, 0)$  for each city, is

$$J_{(I_A^1, \dots, I_S^\Phi)} = \begin{bmatrix} a_A^1 - (b_A^1 + c_A^1) & a_A^1 & 0 & 0 & \dots & 0 & 0 \\ a_S^1 & a_S^1 - (b_S^1 + c_S^1) & 0 & 0 & \dots & 0 & 0 \\ 0 & 0 & a_A^2 - (b_A^2 + c_A^2) & a_A^2 & \dots & 0 & 0 \\ 0 & 0 & a_S^2 & a_S^2 - (b_S^2 + c_S^2) & \dots & 0 & 0 \\ \vdots & \vdots & \vdots & \vdots & \ddots & 0 & 0 \\ 0 & 0 & 0 & 0 & \dots & a_A^\Phi - (b_A^\Phi + c_A^\Phi) & a_A^\Phi \\ 0 & 0 & 0 & 0 & \dots & a_S^\Phi & a_S^\Phi - (b_S^\Phi + c_S^\Phi) \end{bmatrix} \tag{4}$$

Then, the Jacobian matrix is decomposed into two components: the transmission part, denoted as  $T$ , which captures the production of new infections, and the transition part, denoted as  $\Sigma$ , which accounts for changes in the infected states (Diekmann et al. 2010). Specifically, the transition part applies solely to the infected states. Utilizing these matrices, we compute the dominant eigenvalue, also known as the spectral radius, denoted as  $\rho$ , of the matrix  $-T\Sigma^{-1}$ . Hence, we have the following expression:

$$T = \begin{bmatrix} a_A^1 & a_A^1 & 0 & 0 & \dots & 0 & 0 \\ a_S^1 & a_S^1 & 0 & 0 & \dots & 0 & 0 \\ 0 & 0 & a_A^2 & a_A^2 & \dots & 0 & 0 \\ 0 & 0 & a_S^2 & a_S^2 & \dots & 0 & 0 \\ \vdots & \vdots & \vdots & \vdots & \ddots & 0 & 0 \\ 0 & 0 & 0 & 0 & \dots & a_A^\Phi & a_A^\Phi \\ 0 & 0 & 0 & 0 & \dots & a_S^\Phi & a_S^\Phi \end{bmatrix}$$

and

$$\Sigma = \begin{bmatrix} -(b_A^1 + c_A^1) & 0 & 0 & 0 & \dots & 0 & 0 \\ 0 & (b_S^1 + c_S^1) & 0 & 0 & \dots & 0 & 0 \\ 0 & 0 & (b_A^2 + c_A^2) & 0 & \dots & 0 & 0 \\ 0 & 0 & 0 & (b_S^2 + c_S^2) & \dots & 0 & 0 \\ \vdots & \vdots & \vdots & \vdots & \ddots & 0 & 0 \\ 0 & 0 & 0 & 0 & \dots & -(b_A^\Phi + c_A^\Phi) & 0 \\ 0 & 0 & 0 & 0 & \dots & 0 & -(b_S^\Phi + c_S^\Phi) \end{bmatrix}$$

The eigenvalues of  $-T\Sigma^{-1}$  are:  $a_A^i / (b_A^i + c_A^i) + a_S^i / (b_S^i + c_S^i)$ , for  $i = 1, 2, \dots, \Phi$ . Then,  $R_0$  is given by

$$R_0 = \max_{1 \leq i \leq \Phi} \left( \frac{a_A^i}{b_A^i + c_A^i} + \frac{a_S^i}{b_S^i + c_S^i} \right). \tag{5}$$

Since the disease parameters ( $PC_A, PC_S, PD_A, PD_S, PN, k$ ) are equal and the contact rate ( $C, r$ ) is uniform across all cities, the condition  $R_0^i < 1$  for all  $i$  implies  $R_0 < 1$ , leading to local asymptotic stability of the Disease-Free Equilibrium (DFE). Conversely, if  $R_0^i > 1$  for all  $i$ , then  $R_0 > 1$ , indicating the instability of the DFE. This finding aligns with the specific case examined in the study by Arino and Van Den Driessche (2003), where the influence of mobility between cities does not affect the value of  $R_0$ .

### 2.3 The network of cities

The main objective of this study is to propose a novel model in which  $\Phi$  cities are interconnected through a network that reflects the physical transportation infrastructure, including roads, buses, and train lines. In this model, each city is represented as a node in the network, and the edges symbolize the movement of individuals between two cities. The rate of individuals traveling from one city to another is denoted as  $\theta$ . Consequently, within the framework of the PCA simulation for all cities in the network, at the beginning of a time-step, a quantity of  $\theta$  individuals is exchanged between every pair of connected cities, thereby illustrating the intercity trips undertaken by individuals. A time-step is deemed complete when all individuals in this configuration have contacts with neighbors, return to original cities and the states are synchronously updated at the end of the time-step.

The networks under discussion in this paper serve as representations of interconnected cities. Two models of undirected networks will be considered, namely the small-world and Barabási–Albert models, with a fixed size of  $\Phi$  nodes. To construct these networks, the parameters will be systematically varied to encompass a suitable range of topological characteristics. The generation of these networks and the extraction of their topological properties are facilitated by employing the iGraph library (Csardi and Nepusz 2006).

In the case of the small-world model (SW), we begin with a regular network in which each node is connected to  $m_{sw}$  neighbors. Subsequently, each edge is randomly rewired to a different node with a probability of  $p_{sw}$ . On the other hand, the Barabási–Albert (BA) model involves determining the probability, denoted by  $\pi_{ba}(k_i)$ , of selecting a node  $i$  with degree  $k_i$  to form an edge. This probability follows a non-linear preferential attachment mechanism, given by  $\pi_{ba}(k_i) = (k_i / \sum_{j=1}^{m_{ba}} k_j)^{\gamma_{ba}}$ , where  $m_{ba}$  nodes are selected accordingly. The exponent  $\gamma_{ba}$  influences the attachment probability, and when  $\gamma_{ba} = 1$ , it corresponds to the linear and traditional form of the Barabási–Albert (BA) model (Barabási and Albert 1999). In the iGraph library, the input parameters for generating these networks are  $m_{sw}$ ,  $p_{sw}$ ,  $\gamma_{ba}$ , and  $m_{ba}$ .

We conducted an analysis of various network measures to characterize the simulated networks, including the average clustering coefficient, number of edges, shortest path length, density, and diameter. Among these measures, the clustering coefficient emerged as a particularly effective metric for examining the simulation results. In the context of a network comprising a set of vertices  $V$  and a set of edges  $E$ , where an edge  $e_{ij}$  connects nodes  $v_i$  and  $v_j$ , the neighborhood  $n_i$  of a node  $v_i$  is defined as the set of nodes with which node  $i$  shares an edge. For an undirected network,  $n_i$  can be represented as  $n_i = v_j : e_{ij} \in E$ . The clustering coefficient of a node  $i$  reflects the fraction of potential edges among its  $k_i(k_i - 1)/2$  neighbors (Boccaletti et al. 2006). Mathematically, the clustering coefficient can be expressed as follows:

$$g_{cc}^i = \frac{2|e_{jk} : v_j, v_k \in n_i, e_{jk} \in E|}{k_i(k_i - 1)}$$

and the average clustering coefficient can be written as  $g_{cc} = \frac{1}{|V|} \sum_{i=1}^{|V|} C_i$ .

Concerning measures of graph centralization, the study considered several centrality measures, namely betweenness, closeness, degree, and eigenvector centrality (Boccaletti et al. 2006). As the results yielded similar outcomes across these parameters, the degree centrality, which denotes the number of edges connected to a node, was chosen as the basis for comparison due to its simplicity. Following the determination of centrality, the centralization index at the graph level was calculated as the sum of the deviations from the maximum degree



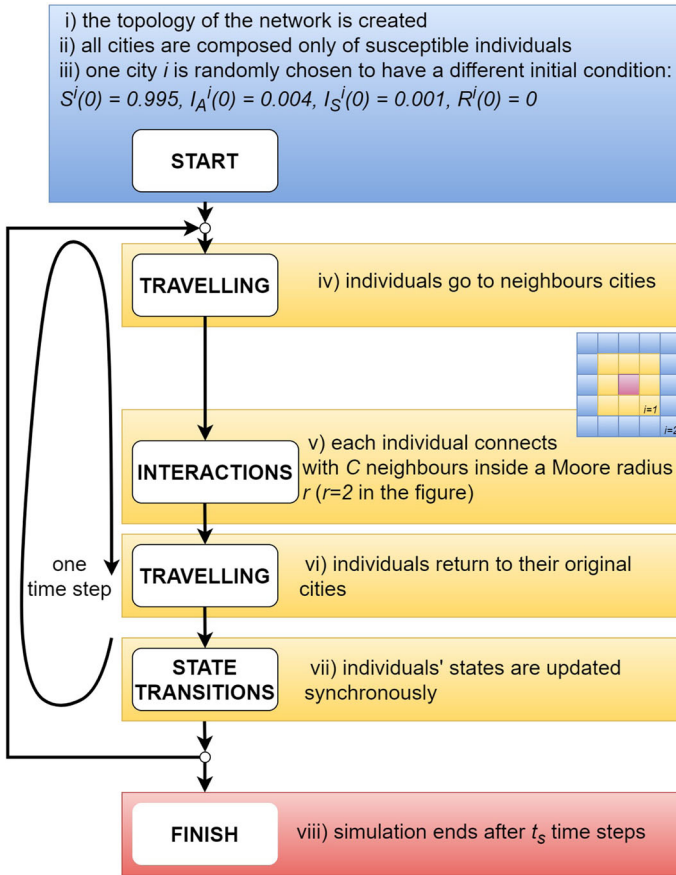


Fig. 1 Simulation diagram of the model

centrality. Consequently, a higher centralization index indicates a more centralized graph structure. For the purpose of denoting the centralization derived from the degree centrality of the nodes, the symbol  $g_{deg}$  is employed.

### 2.4 Simulation summary

Therefore, each simulation entails the generation of a network based on the specified network parameters. Initially, all cities within the network are assigned exclusively susceptible individuals. Subsequently, a single city is randomly selected to serve as the origin of the disease outbreak, wherein infected individuals are introduced into the initial state. Each time-step of the simulation involves the movement of individuals to neighboring cities, adhering to the defined rules and  $\theta$ . Then, individuals engage in interactions with their respective neighborhoods. Following this, individuals return to their original cities, and state transitions occur, with the synchronous updating of individual states transpiring at the conclusion of each time-step. An overview of a simulation of the model is presented in Fig. 1.

### 3 Results

In this section, we present the simulation results, which are divided into the following subsections:

- 3.1 Simulation of the model for a single city.
- 3.2 Visualization of disease spreading across selected network examples. This includes the depiction of network images and the temporal evolution of infected individuals in different cities.
- 3.3 Simulations conducted with a diverse range of network input parameters to explore networks with varying properties.
- 3.4 Repeated simulations from the previous subsection, but with the variation of the infectivity parameter  $k$  to determine the minimum value necessary for the disease to propagate throughout the entire network of cities.
- 3.5 Use of the data obtained from the previous subsection to analyze the relationship between the basic reproduction number and variables  $k$  and  $\theta$ .

The epidemiological parameters utilized in this study are estimations derived from the initial waves of the COVID-19 pandemic. Consequently, a time-step equivalent to 1 day is adopted, and the recovery periods for asymptomatic and symptomatic infected individuals are estimated to be 10 and 14 days, respectively, yielding  $P_{C_A} = 1/10$  and  $P_{C_S} = 1/14$ . It is assumed that asymptomatic individuals do not experience mortality directly attributable to the disease, while approximately 1% of symptomatic individuals may succumb to disease complications. Thus, we set  $P_{D_A} = 0$  and  $P_{D_S} = 0.01$  to reflect these probabilities. Considering an average life expectancy of 78 years (based on Brazilian data) and assuming immunity lasts for four months (or until a new variant is introduced to the population), the probability  $P_N$  is calculated as  $1/(78 \times 365) + 1/120 \approx 0.00837$ . The parameter values are derived from relevant studies (Gostic et al. 2020; Ma et al. 2020; Wu et al. 2020). Moreover, it is assumed that 20% of new infections manifest as symptomatic cases, while the remaining 80% are asymptomatic. Lastly, the values of  $C$ ,  $r$ , and  $k$  are adjusted to yield an estimated  $R_0$  within the range of 1–6, as reported in previous studies (Gostic et al. 2020; Singhal 2020; Zhou et al. 2020). Consequently, we set  $C = 4$ ,  $r = 4$ , and  $k = 0.1$ . A summary of the input parameters is provided in Table 1.

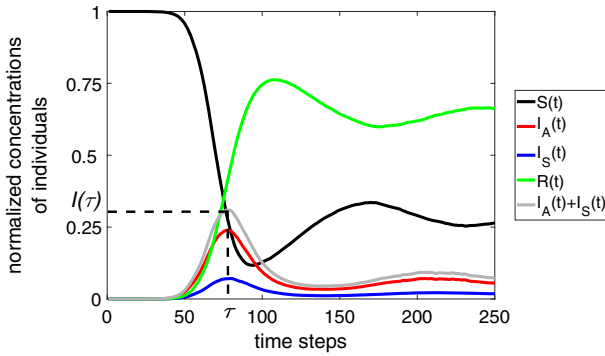
It is worth noting that additional parameters were examined in the simulations. The probabilities of recovery and mortality were chosen in accordance with values commonly employed in the literature for analogous models. Simulations incorporating slightly different values for  $P_{C_A}$ ,  $P_{C_S}$ ,  $P_{D_A}$ ,  $P_{D_S}$ , and  $P_N$  exhibited similar trends in the transient behavior of the infected individuals curve, with variations primarily observed in the concentrations of the different disease states during the steady state. However, the variables associated with the infection process ( $C$ ,  $r$ , and  $k$ ) exerted a more pronounced influence. Notably, higher values of disease infectiousness within the population resulted in earlier peaks of infected states during the simulation's initial stages. Furthermore, depending on the magnitude of these variables and  $\theta$ , the peaks in the cities tended to synchronize during these early stages.

#### 3.1 Simulation for one city

The first result of this study involves the simulation of the PCA model for a single city, which is not connected to any other cities. The lattice size is set to  $200 \times 200$ , accommodating a total of  $N = 40,000$  cells. The initial conditions are as follows:  $S(0) = 0.995$ ,  $I_A(0) = 0.004$ ,  $I_S(0) = 0.001$ , and  $R(0) = 0$ . The initial states are randomly distributed across the lattice.

**Table 1** Description of input parameters used for PCA model. \*Note that C, r and k were chosen to have an  $R_0$  value within the range of [1, 6]

Parameter	Description	Value	References
$\Phi$	Number of cities in the network	–	–
$\theta$	Number of travelers per city per edge of the network	–	–
$m_{sw}, p_{sw}$	Parameters for creating small-world networks	–	–
$\gamma_{ba}, m_{ba}$	Parameters for creating Barabási–Albert networks	–	–
$n$	Lattice side	200	–
$N$	Total number of cells	40,000	–
$k$	Infectivity parameter	0.1	*Gostic et al. (2020), Singhal (2020) and Zhou et al. (2020)
$P_{CA}$	Probability of cure of asymptomatic infected individuals	1/10	Ferguson et al. (2020), Hu et al. (2020) and Singhal (2020)
$P_{CS}$	Probability of cure of symptomatic infected individuals	1/14	Ferguson et al. (2020), Hu et al. (2020) and Singhal (2020)
$P_{DA}$	Probability of dying due to disease for asymptomatic infected individuals	0	Ferguson et al. (2020), Hu et al. (2020) and Singhal (2020)
$P_{DS}$	Probability of dying due to disease for symptomatic infected individuals	0.01	Ferguson et al. (2020), Hu et al. (2020) and Singhal (2020)
$P_N$	Probability of dying due to other causes	0.00837	IBGE (2021)
$C$	Number of contacts per individual	4	*Gostic et al. (2020), Singhal (2020) and Zhou et al. (2020)
$r$	Maximum radius for contact in the lattice	4	* Gostic et al. (2020), Singhal (2020) and Zhou et al. (2020)
$S^i(0)$	Number of susceptible individuals in city $i$ at time $t = 0$	–	–
$I_A^i(0)$	Number of asymptomatic infected individuals in city $i$ at time $t = 0$	–	–
$I_S^i(0)$	Number of symptomatic infected individuals in city $i$ at time $t = 0$	–	–
$R^i(0)$	Number of recovered individuals in city $i$ at time $t = 0$	–	–



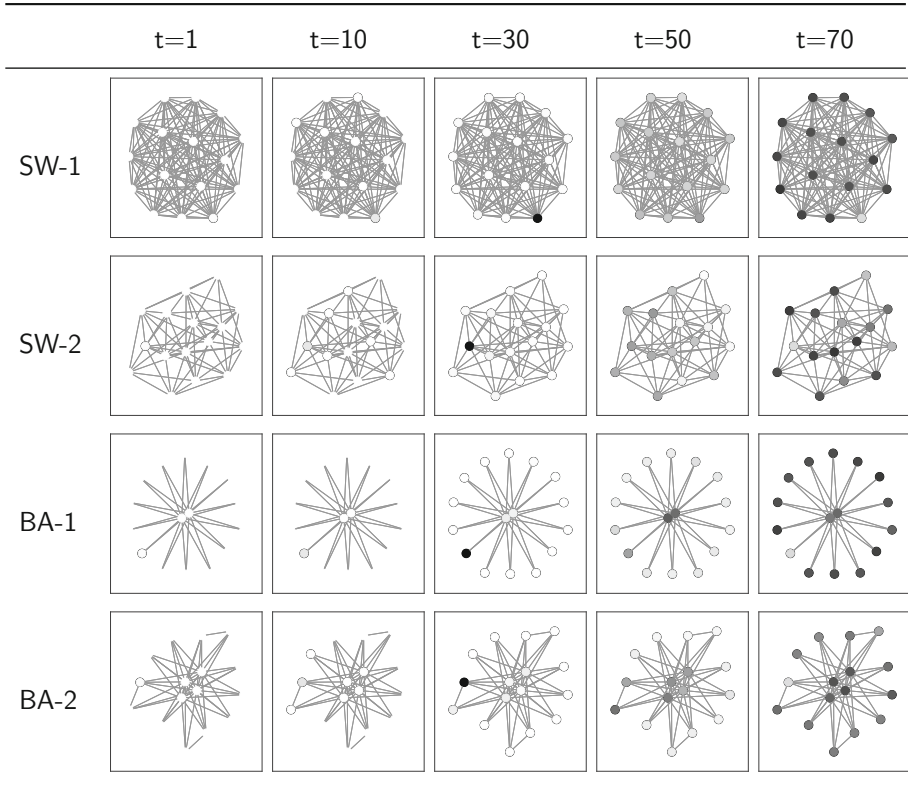
**Fig. 2** Time evolution of susceptible, asymptomatic and symptomatic infected, and recovered individuals for one city with no connection to other cities. The point indicated by  $I(\tau)$  and  $\tau$  is the peak of infected individuals in the simulation and the instant when it occurred

Figure 2 displays the temporal evolution of the simulation for the four states over a duration of  $t_s = 250$  time-steps. It is worth noting that the time-step at which the peak of infected individuals  $I(\tau)$  occurs is denoted as  $\tau$ . In this case,  $\tau$  is found to be 78, with a corresponding value of  $I(\tau) = 0.32$ . Furthermore, in the equilibrium state (occurring after time-step 350, not depicted in the figure), the calculated value of the basic reproduction number  $R_0$  is 3.61. This value is obtained by averaging the values of  $a_A, a_S, b_A, b_S, c_A,$  and  $c_S$  over the last 20 time-steps.

### 3.2 Simulations for a network of cities

When simulating a network of cities, there exist differences in the initial conditions. Specifically, only one random city, denoted as  $i$ , begins with the following initial values:  $S^i(0) = 0.995, I_A^i(0) = 0.004, I_S^i(0) = 0.001,$  and  $R^i(0) = 0$ . These values are uniformly distributed over the lattice of that particular city. Figure 3 presents a simulation for each type of network at time instants  $t = 1, t = 10, t = 30, t = 50,$  and  $t = 70$ . The networks were created with the following parameters:  $\Phi = 16$  for all networks,  $m_{sw} = 16$  and  $p_{sw} = 0.35$  for small-world-1,  $m_{sw} = 4$  and  $p_{sw} = 0.95$  for small-world-2,  $m_{ba} = 2$  and  $\gamma_{ba} = 4.8$  for Barabási–Albert-1, and  $m_{ba} = 4$  and  $\gamma_{ba} = 2.9$  for Barabási–Albert-2. A city with no infected cases is depicted without a border. As the disease begins to spread within a city, a black line border is displayed, and a black-filled node represents the peak number of infected individuals in that city. The grayscale intensity is proportional to the number of infection cases. The proportion of individuals traveling per time-step in this study is  $\theta = 50$ .

The graphs presented in Fig. 3 provide preliminary evidence suggesting asynchronous occurrence of disease peaks across the cities. Prior to conducting a comprehensive analysis of this phenomenon, Fig. 4 illustrates the temporal evolution of the number of infected individuals for four randomly generated networks, each with two different values of the traveling rate denoted as  $\theta$ . The colored lines represent the normalized concentration of infected individuals ( $I_A(t) + I_S(t)$ ) in each city. It is noteworthy that simulations with smaller values of  $\theta$  exhibit delayed and reduced peaks in the number of infected cases. Conversely, simulations with  $\theta = 50$  demonstrate synchronized peaks across cities. Specifically, the small-world (SW) instance represents a fully connected network characterized by a clustering coefficient of 1 and zero centralization, while the Barabási–Albert (BA) instance depicts a centralized



**Fig. 3** Infection cases in four networks for time-steps  $t = 1, t = 10, t = 30, t = 50,$  and  $t = 70$ . The parameters for creating the networks were  $\Phi = 16; m_{sw} = 16$  and  $p_{sw} = 0.35$  for small-world-1;  $m_{sw} = 4$  and  $p_{sw} = 0.95$  for small-world-2;  $m_{ba} = 2$  and  $\gamma_{ba} = 4.8$  for Barabási–Albert-1, and  $m_{ba} = 4$  and  $\gamma_{ba} = 2.9$  for Barabási–Albert-2. The traveling rate is  $\theta = 50$ . A city with no infected case has no border. A node filled in black represents the peak of infected individuals for that city, and the grayscale is proportional to the infection cases

network with a low clustering coefficient and high centralization. These outcomes underscore the necessity of simulating a diverse range of networks to comprehend the dynamic behavior of the disease within the entire population.

The relevant output variables analyzed in this study are presented in Table 1. It is important to note that we define  $I(t) = \sum_{i=1}^{\Phi} I_A^i(t) + I_S^i(t)$ , which represents the time series of infected individuals for the entire network. Within this notation, the variable  $\tau$  denotes the time instant at which the maximum value of the temporal series  $I(t)$  is observed (Table 2). Additionally, we consider another variable, the standard deviation of the peak infected cases across cities, denoted as  $\sigma$ .

### 3.3 A complete set of networks

The objective here is to construct networks encompassing a broad spectrum of topological parameters within a given model, in order to assess the impact of network properties on the maximum number of infected individuals, the timing of the peak, and the standard deviation of

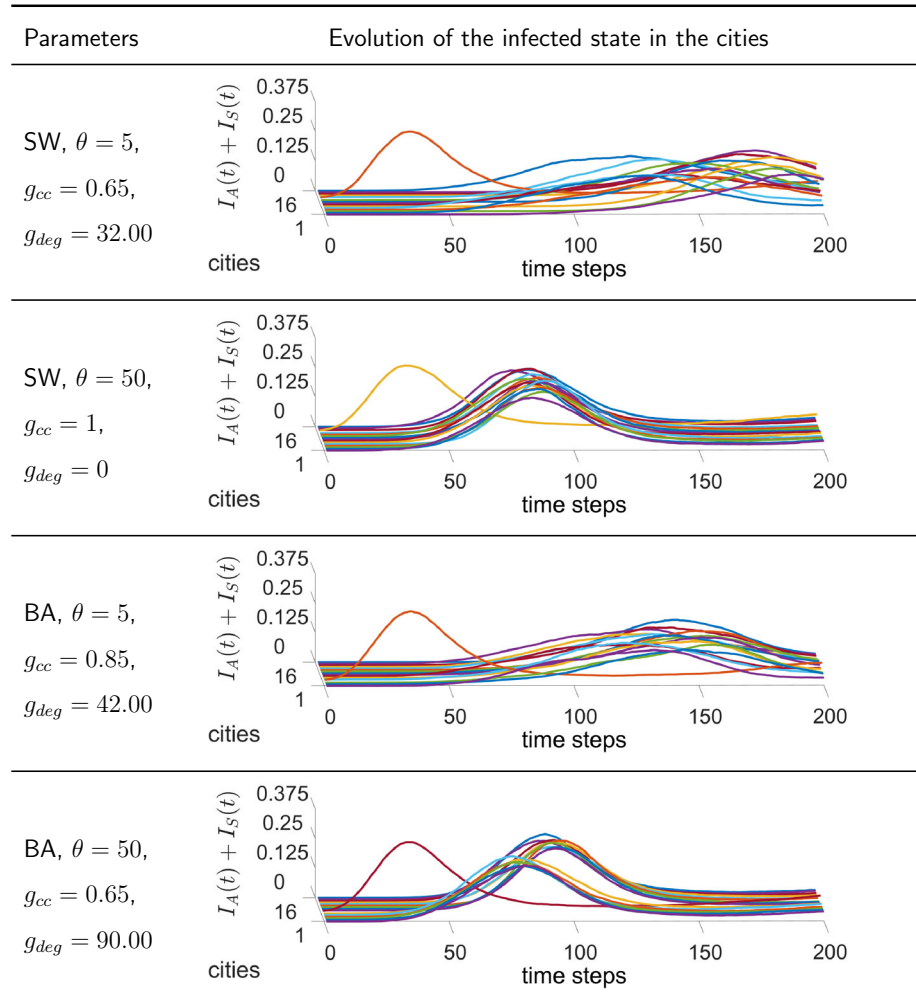


**Fig. 4** Time evolution of infected individuals ( $I_A^i(t) + I_S^i(t)$ ) of all cities  $i$  for two small-world and two Barabási–Albert networks, along with respective traveling rate, clustering coefficient and degree centralization. Each color represents a city (color figure online)

**Table 2** Description of the output variables

Parameter	Description
$\tau$	Instant when the peak of infected individuals occurs for the entire network
$I(\tau)$	Peak of infected individuals for the entire network
$\sigma$	Standard deviation of the cities' peak of infected
$g_{cc}$	Clustering coefficient of the network
$g_{deg}$	Degree centrality of the network

peak values across cities. The networks were constructed and their topological properties were obtained using the iGraph library (Csardi and Nepusz 2006). Subsequently, 1000 simulations per network were conducted by running twenty simulations for each value of the traveling rate,  $\theta$ , where  $\theta$  takes on values ranging from 1 to 50. These simulations run for  $t_s = 500$  to guarantee that the system achieves the permanent regime. Random input network parameters were utilized in each simulation. For the small-world network model, the number of close neighbors connected to each node, denoted as  $m_{sw}$ , and the fraction of rewired connections, denoted as  $p_{sw}$ , were randomly selected within the intervals  $2 \leq m_{sw} \leq 16$  and  $0 \leq p_{sw} \leq 1$ , respectively. In the case of the Barabási–Albert network model, the number of connections generated per node, represented by  $m_{ba}$ , and the exponent of the probability of a node being selected to receive an edge, denoted as  $\gamma_{ba}$ , were randomly chosen within the intervals  $2 \leq m_{ba} \leq 16$  and  $1 \leq \gamma_{ba} \leq 5$ . It is important to note that only connected networks were considered in the analysis.

Therefore, Fig. 5 illustrates the peak of infected individuals ( $I(\tau)$ ) for all cities as a function of the clustering coefficient (Fig. 5a, c), degree centralization (Fig. 5b, d), and the traveling rate. The simulations are performed on small-world networks (Fig. 5a, b) and Barabási–Albert networks (Fig. 5b, d). The time instant of the peak ( $\tau$ ) for the entire network and the standard deviation of the peak time for each city are depicted in Figs. 6 and 7, respectively, corresponding to the same categories as presented in Fig. 5.

Consider Figs. 5, 6, and 7. When a network with a control parameter of  $\theta = 50$  regulates the flow of travelers among cities and the travel rate is reduced to  $\theta = 25$ , the peak of infected individuals in the network, denoted as  $I(t)$ , decreases from approximately 0.32 to 0.25, resulting in a reduction of 22% in the peak value. Furthermore, the occurrence of this peak is delayed from approximately  $\tau \approx 75$  to  $\tau \approx 105$ , and the standard deviation of the peaks in the cities increases.

Analyzing these same figures, it becomes evident that the primary factor contributing to the flattening of the infected cases curve, thus reducing and delaying the peak, is the traveling rate parameter  $\theta$ . Another factor that has a minor influence on the infected cases curve is the clustering coefficient for small-world networks (subfigures a). The small-world model, originally proposed by Watts and Strogatz (1998), can generate networks with small-world properties, as well as random and random regular networks when the rewiring probability is low. As a result, it allows for uniform neighborhood connections, which increases the clustering coefficient. This effect enhances the propagation of the disease by increasing the peak value of infected cases  $I(\tau)$ , decreasing the time of occurrence  $\tau$ , and causing the peak to happen within a narrower time frame in the cities. It was the simultaneous occurrence of this peak at the early stages of the COVID-19 pandemic that led to a surge in cases, overwhelming healthcare systems in many countries (Ferguson et al. 2020; Tanne et al. 2020; Verelst et al. 2020). Conversely, none of the topological parameters calculated from the Barabási–Albert model networks significantly influenced the evolution of infected cases during the initial time-steps of the simulation. Additionally, the network centralization did not affect this transient phase.

### 3.4 Quantifying infectivity levels and disease spreading for the entire network

In this section, we aim to examine the influence of the parameter  $k$ , which represents the infectivity of the disease, on the spread of the disease within the network of cities. Specifically, we investigate the minimum value of  $k$  required for the disease to affect all cities in the network. To achieve this, we conduct twenty simulations for each value of  $k = 50, 49, 48, \dots, 22, 21, 20$ ,

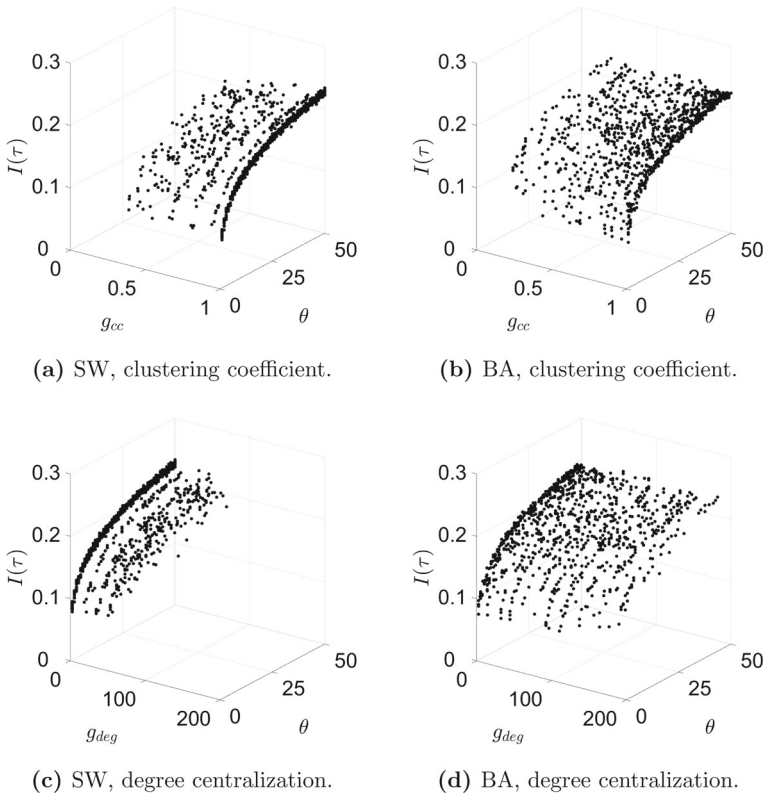


**Fig. 5** Peak of infected individuals for the entire cities network in function of the clustering coefficient (a, c), degree centralization (b, d) and the traveling rate. Results for small-world (a, b) and Barabási–Albert (b, d) networks simulations

employing randomly selected parameters using the same process as the previous simulation set. For the small-world network, we consider  $2 \leq m_{sw} \leq 16$  and  $0 \leq p_{sw} \leq 1$ , while for the Barabási–Albert network, we consider  $2 \leq m_{ba} \leq 16$  and  $1 \leq \gamma_{ba} \leq 5$ . Only connected networks are considered. Using the simulation data, we determine the minimum  $k$  values based on  $\theta$ , clustering coefficient intervals, and degree centralization, as illustrated in Fig. 8.

Figure 8 presents the minimum infectivity parameter  $k$  required for the disease to propagate throughout the entire network of cities, in relation to the clustering coefficient (Fig. 8a, b), degree centralization (Fig. 8c, d), and the traveling rate. It is noteworthy that networks with higher clustering coefficients, indicating greater interconnectedness, and lower centralization, denoting more uniform connections among nodes, necessitate lower values of the infectivity parameter  $k$  for the disease to spread across the entire network of cities. Conversely, networks exhibiting higher centralization tend to exhibit similar levels of the minimum  $k$  value. Therefore, disease propagation throughout the network is facilitated in highly interconnected or centralized city networks, where diseases with lower infectivity parameter values can propagate to all cities effectively. Consequently, reducing the traveling rate implies that diseases must possess higher values of  $k$  to achieve widespread transmission.



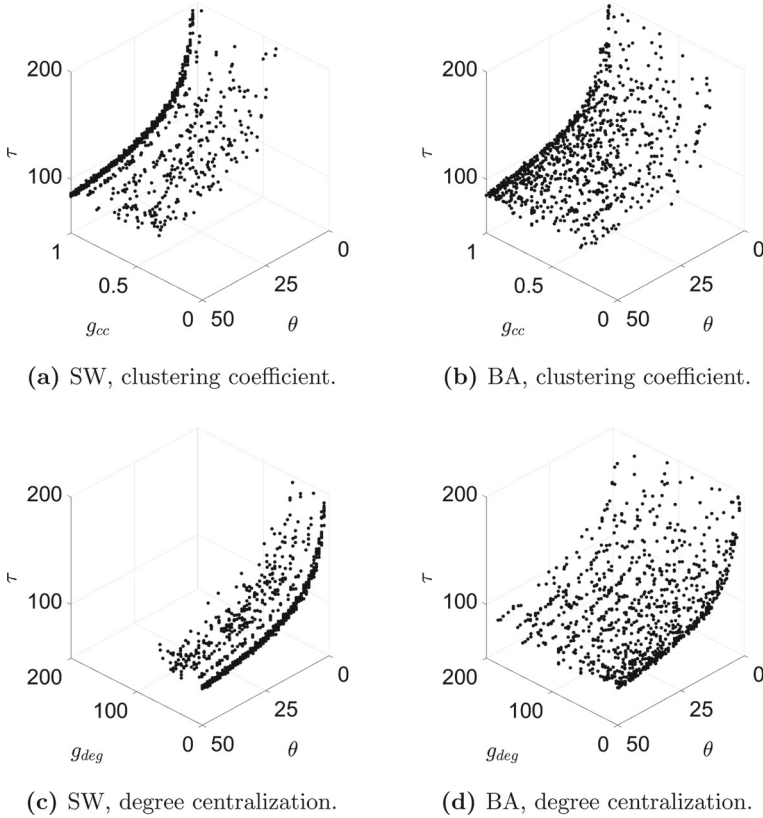


**Fig. 6** Instant of peak of infected individuals for the entire cities network in function of the clustering coefficient (a, c), degree centralization (b, d) and the traveling rate. Results for small-world (a, b) and Barabási–Albert networks simulations

### 3.5 The basic reproduction number

The determination of the basic reproduction number for a network comprising equal-sized cities, characterized by uniformity in shape, population size, epidemiological parameters, and interconnections among individuals, was established in Arino and Van Den Driessche (2003). According to the analysis presented in Sect. 2 and expressed by Eq. (1), this definition posits that the highest value of the reproduction number ( $R_0$ ) among the patches serves as an indicator of disease propagation within the population. It is important to note that  $R_0$  is solely dependent on the disease situation within cities that have reported cases. However, it may not accurately reflect the dynamics occurring across the network, as the disease may be endemic in certain cities without spreading to the entirety of the network (it is worth mentioning that only connected networks were considered in this study).

Consequently, by considering the average value of  $R_0$  across all cities ( $\overline{R_0}$ ), we can have insights into the absence of disease transmission across some patches. Figure 2, which corresponds to the same simulation setup as before, depicts  $\overline{R_0}$  as a function of the travel rate ( $\theta$ ) and the infectivity parameter ( $k$ ). Notably, higher travel rates are associated with a discernible step-wise increase in  $\overline{R_0}$ , indicating an endemic state of the disease across the majority of

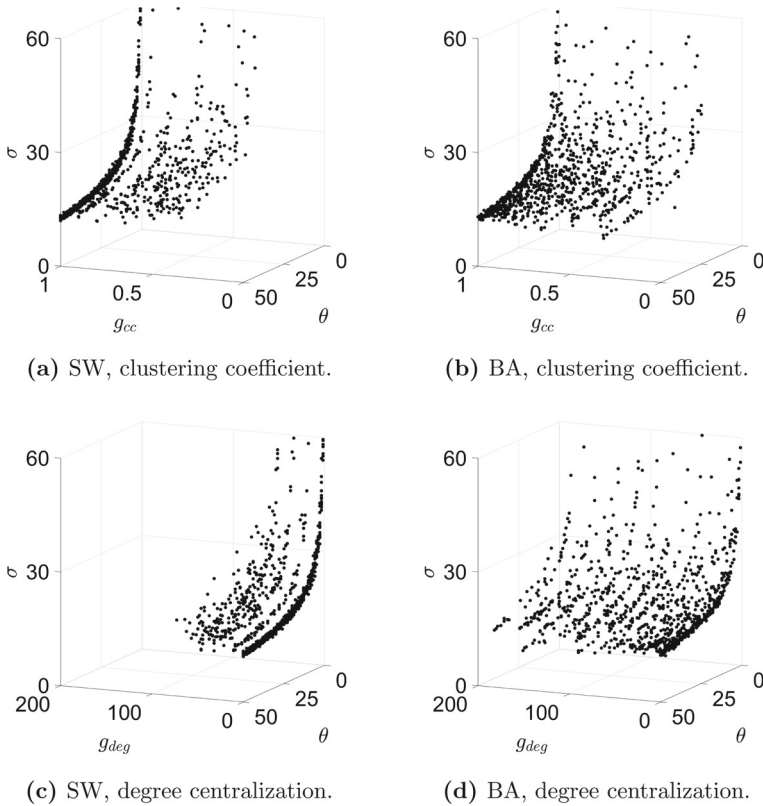


**Fig. 7** Standard deviation of the instant of peak of infected individuals on each city in function of the clustering coefficient (a, c), degree centralization (b, d), and the traveling rate. Results for small-world (a, b) and Barabási–Albert networks simulations

cities. Conversely, lower travel rates correspond to diminished values of  $\overline{R_0}$ , not because the disease is inherently less severe, but rather due to its limited spread among cities.

This is an important result, because it contains data from all small-world and Barabási–Albert networks simulated. If the analytical analysis of the system returns that the  $R_0$  of the system is the maximum value among cities, Fig. 9 shows that the average value of the basic reproduction number in the network is a function only of  $k$  and  $\theta$ . If previous results showed that reducing the individuals’ travel rates among cities can flatten the infected curve, here we can see that such reduction can also prevent the disease to achieve every city, reducing  $\overline{R_0}$ .

### 4 Discussion

In this paper, we present a novel multi-patch model that investigates the propagation of diseases in random networks of interconnected cities. By incorporating local interactions within cities and the traveling rate among them, we examine how network topologies influence disease outbreaks and their subsequent evolution. We extend existing city connection models by considering two types of random networks: small world and Barabási–Albert. The progression of disease spread across the network is dependent on both the network topol-

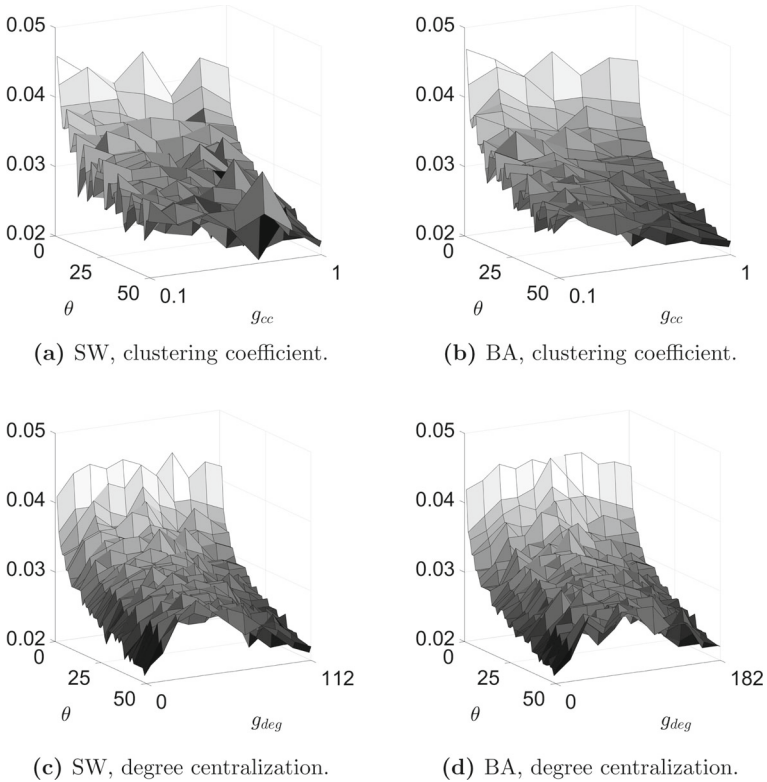
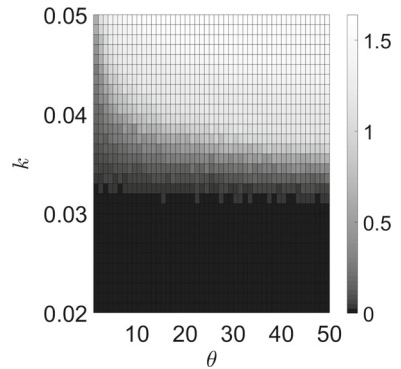


**Fig. 8** Minimum value of  $k$  required for the disease to spread in all the cities in the network in function of the clustering coefficient (a, b), degree centralization (c, d) and the traveling rate

**Fig. 9** Average basic reproduction number for all the cities ( $\bar{R}_0$ ) in function of the traveling rate ( $\theta$ ) and the infectivity parameter ( $k$ )



ogy and the rate at which individuals travel. Our findings reveal that networks characterized by high traveling rates experience an earlier and more extensive peak of infections, which occurs almost simultaneously across all cities. Conversely, networks with lower traveling rates exhibit a delayed and reduced peak of infections, manifesting at different time-steps across the cities. This disparity in outbreak peaks aligns with observations made in models

that incorporate spatially distributed subpopulations, such as the study investigating contact patterns in Russian cities by Leonenko et al. (2020).

Topological parameters of the network, including the clustering coefficient and the centralization degree, do not provide direct insights into the dynamics of infected cases, except for small-world networks where the clustering coefficient can offer some information regarding the peak of infected cases, denoted as  $I(t)$  (see Fig. 5a). However, these parameters can be employed to assess the likelihood of disease dissemination across all cities within the network. As demonstrated in Fig. 8, highly interconnected networks characterized by a high clustering coefficient and a low centralization degree necessitate lower values of the infectivity parameter  $k$  to facilitate the spread of the disease to all cities. Conversely, networks with fewer connections (thus exhibiting a low clustering coefficient) and a low centralization degree require a more transmissible disease (higher  $k$ ) for it to pervade the entire network.

The analysis of network parameters presented in this manuscript has been made possible by the inclusion of a larger network size. This enlarged network has allowed for meaningful insights into the spread of disease across the network in relation to its infectivity parameter, emphasizing the significance of considering the topology of patches when planning control strategies. Certain results remain consistent regardless of the network size, such as the observed delay in the infection curve between the city with the initial case and the other cities (Salmani 2006; Arino et al. 2007; Cui et al. 2017), the effectiveness of global control measures impacting all patches (Zakary et al. 2017), and the analysis of synchronized and desynchronized infection curves among patches (Nipa and Allen 2020). However, given the homogeneity of the patches in this study, the influence of variations among the patches (e.g., susceptible and infected travel rates, epidemiological parameters) (Chen et al. 2020; Mpolya et al. 2014; Prosper et al. 2012),  $R_0$  is a function only of the epidemiological parameters of a single city within the network, even if the value is the same for all cities when the disease spreads throughout the entire network.

Other studies have indicated that in a multi-city model, the basic reproduction number ( $R_0$ ) serves as an indicator of disease endemicity within the population (Arino and Van Den Driessche 2003). The extension of  $R_0$  from a single city to a multi-city environment aids in assessing the global stability of the disease (Arino and Van Den Driessche 2003; Kheiri and Jafari 2019; Wang and Zhao 2006). In this study, we consider two values for  $R_0$ :  $R_0 = 0$  for the disease-free scenario and  $R_0 > 1$  for the endemic situation, where  $R_0$  remains the same for all cities within the network. Figure 9 illustrates this relationship for higher values of the traveling rate ( $\theta$ ), representing the presence of the disease in every city. It is worth noting that in Schimit and Monteiro (2009), a very similar model was applied to a single city, and they found that both the number of connections individuals make per time-step ( $C$ ) and the maximum connection radius ( $r$ ) influence the value of  $R_0$  in the system.

Therefore, simulation studies have suggested that if the disease exhibits an initial reproduction number  $R_0 > 1$ , implementing interventions at the micro-level can effectively reduce  $R_0$  by decreasing local contacts between individuals. On the other hand, macro-level interventions are instrumental in delaying and mitigating the infection peak on a global scale, a strategy commonly referred to as “flattening the curve.” This approach gained significant attention during the early stages of the global COVID-19 pandemic as a means of reducing the strain on healthcare systems caused by a high number of infected individuals (Verelst et al. 2020). At the micro-level, control measures can be implemented by reducing the infectivity parameter  $k$ , for instance, through the use of masks and practising social distancing. These actions effectively decrease the number of contacts  $C$  between individuals, resulting in a similar reduction of  $R_0$ . Conversely, at the macro-level, control measures focus on reducing the traveling rate  $\theta$ , thereby flattening the curve of infections and subsequently decreasing

the magnitude and delaying the occurrence of the infection peak. Furthermore, even within the context of the network of cities considered in this study, with equal population sizes, it is crucial to concentrate efforts on central cities to effectively combat the outbreak of the pandemic. In networks characterized by higher centralization, even a lower level of infectivity is sufficient for the disease to trigger an epidemic outbreak in all cities. This effect becomes even more pronounced in metropolitan areas where central cities tend to have larger populations.

In Xi et al. (2020), the authors demonstrate a significant correlation between mobility and the transmission of COVID-19 in China. They found that a reduction in human mobility was followed by a decline in transmission, with an average lag time of 10 days. Notably, cities with high influxes of individuals from Wuhan exhibited shorter lag periods, highlighting the importance of adopting multi-city approaches to disease control. Fiocruz's technical notes (Notas 2022) (Technical Note 15-December 18th) report a synchronization of epidemic curves in Brazil in 2020, following the expansion of COVID-19 cases in smaller cities and rural areas. According to the same report, it was estimated that an 80% reduction in mobility in metropolitan regions could decrease the basic reproduction number ( $R_0$ ) from 2.5 to 1.7 and delay the peak of infections by up to 75 days.

The role of vaccination in the context of individual mobility across different patches during an infectious disease outbreak is of paramount importance. However, in the absence of interregional coordination, regions surrounded by non-vaccinated populations necessitate heightened efforts (Klepac et al. 2016). Moreover, individuals may engage in strategic decision-making when choosing their travel destinations based on prevailing conditions (Zhao et al. 2018). Incorporating the dynamic decision-making of individuals into the analysis introduces an additional layer of complexity, potentially resulting in patches exhibiting different stages of the outbreak. This underscores the necessity for processes that effectively segment regions while considering a global perspective of the outcomes, as exemplified in the present study.

The subsequent stages of this research aim to extend the scope by considering cities of varying sizes and travel rates to simulate a metropolitan area alongside satellite cities. Furthermore, the utilization of real data will be incorporated to fine-tune the network parameters in the context of the COVID-19 outbreak and to determine optimal strategies for global pandemic control (Balcan et al. 2010). The inherent flexibility of the proposed model enables the exploration and evaluation of diverse aspects explored in multi-city studies, including but not limited to demographic and seasonal variability (Nipa and Allen 2020), the impact of vaccination campaigns (Cui et al. 2017), travel restrictions between cities (Zakary et al. 2017), and the implementation of quarantine measures to reduce interpersonal contacts (Arino et al. 2007).

**Funding** PHTS is supported by grants #440025/2020-6, #307194/2019-1 and #402874/2016-1 of Conselho Nacional de Desenvolvimento Científico e Tecnológico (CNPq) and grant #2017/12671-8, São Paulo Research Foundation (FAPESP).

**Data Availability** The datasets generated during and/or analyzed during the current study are available in the link <https://bit.ly/3MloXCc>. It is not in a repository due to the large size of the files.

## Declarations

**Conflict of interest** The authors declare that there are no conflicts of interest regarding the publication of this paper.

**Ethical approval** Ethics approval was not required for this study.

## References

- Ahmed E, Agiza H, Hassan S (1998) On modeling hepatitis b transmission using cellular automata. *J Stat Phys* 92:707–712
- Allen LJ, Bolker BM, Lous Y, Nevai AL (2007) Asymptotic profiles of the steady states for an SIS epidemic patch model. *SIAM J Appl Math* 67(5):1283–1309
- Anderson RM, May RM (1991) *Infectious diseases of humans: dynamics and control*. Oxford University Press, Oxford Science Publications, Oxford
- Aranha V (2005) Mobilidade pendular na metrópole paulistana. *São Paulo Perspect* 19:96–109
- Arino J, Van Den Driessche P (2003) A multi-city epidemic model. *Math Popul Stud* 10(3):175–193. <https://doi.org/10.1080/08898480306720>
- Arino J, Jordan R, van den Driessche P (2007) Quarantine in a multi-species epidemic model with spatial dynamics. *Math Biosci* 206(1):46–60
- Balcan D, Gonçalves B, Hu H, Ramasco JJ, Colizza V, Vespignani A (2010) Modeling the spatial spread of infectious diseases: the global epidemic and mobility computational model. *J Comput Sci* 1(3):132–145
- Barabási A-L, Albert R (1999) Emergence of scaling in random networks. *Science* 286(5439):509–512
- Boccaletti S, Latora V, Moreno Y, Chavez M, Hwang DU (2006) Complex networks: structure and dynamics. *Phys Rep* 424(4–5):175–308
- Castellazzo A, Mauro A, Volpe C, Venturino E (2012) Do demographic and disease structures affect the recurrence of epidemics? *Math Model Nat Phenom* 7(3):28–39
- Chandrasekaran B, Fernandes S (2020) Since January 2020 Elsevier has created a COVID-19 resource centre with free information in English and Mandarin on the novel coronavirus. The COVID-19 resource centre is hosted on Elsevier Connect, the company's public news and information website. *Diabetes Metab Syndr* 14(4):337–339
- Chen S, Owolabi Y, Li A, Lo E, Robinson P, Janies D, Lee C, Dulin M (2020) Patch dynamics modeling framework from pathogens' perspective: unified and standardized approach for complicated epidemic systems. *PLoS One* 15(10):1–18
- Chinazzi M, Davis JT, Ajelli M, Gioannini C, Litvinova M, Merler S, Pastore y Piontti A, Mu K, Rossi L, Sun K, Viboud C, Xiong X, Yu H, Elizabeth Halloran M, Longini IM, Vespignani A (2020) The effect of travel restrictions on the spread of the 2019 novel coronavirus (COVID-19) outbreak. *Science* 368(6489):395–400
- Cissé B, El Yacoubi S, Gourbière S (2016) A cellular automaton model for the transmission of Chagas disease in heterogeneous landscape and host community. *Appl Math Model* 40(2):782–794
- Colizza V, Barthélemy M, Barrat A, Vespignani A (2007) Epidemic modeling in complex realities. *C R Biol* 330(4):364–374
- Csardi G, Nepusz T (2006) The igraph software package for complex network research. *Int J Complex Syst* 1695:1–9
- Cui Q, Qiu Z, Ding L (2017) An sir epidemic model with vaccination in a patchy environment. *Math Biosci Eng* 14(5–6):1141–1157
- Diekmann O, Heesterbeek J, Roberts MG (2010) The construction of next-generation matrices for compartmental epidemic models. *J R Soc Interface* 7:873–885
- Dorjee S, Revie CW, Poljak Z, McNab WB, Sanchez J (2013) Network analysis of swine shipments in Ontario, Canada, to support disease spread modelling and risk-based disease management. *Prev Vet Med* 112(1–2):118–27
- Ferguson NM, Laydon D, Nedjati-Gilani G, Imai N, Ainslie K, Baguelin M, Bhatia S, Boonyasiri A, Cucunubá Z, Cuomo-Dannenburg G, Dighe A, Dorigatti I, Fu H, Gaythorpe K, Green W, Hamlet A, Hinsley W, Okell LC, Van Elsland S, Thompson H, Verity R, Volz E, Wang H, Wang Y, Gt Walker P, Walters C, Winskill P, Whittaker C, Donnelly CA, Riley S, Ghani AC (2020) Impact of non-pharmaceutical interventions (NPIs) to reduce COVID-19 mortality and healthcare demand, Faculty of Medicine/School of Public Health/Imperial College London, no. March, pp 3–20 (2020)
- Fiocruz (2020) Regiões e redes COVID-19: Acesso aos serviços de saúde e fluxo de deslocamento de pacientes em busca de internação
- Franc A (2004) Metapopulation dynamics as a contact process on a graph. *Ecol Complex* 1(1):49–63
- Gostic KM, Gomez AC, Mummah RO, Kucharski AJ, Lloyd-Smith JO (2020) Estimated effectiveness of symptom and risk screening to prevent the spread of COVID-19. *eLife* 9:2
- Gwizdalła T (2020) Viral disease spreading in grouped population. *Comput Methods Programs Biomed* 197:105715
- Hu Z, Song C, Xu C, Jin G, Chen Y, Xu X, Ma H, Chen W, Lin Y, Zheng Y, Wang J, Hu Z, Yi Y, Shen H (2020) Clinical characteristics of 24 asymptomatic infections with COVID-19 screened among close contacts in Nanjing, China. *Sci China Life Sci* 63:706–711

- IBGE (2021) Tábuas completas de mortalidade, Instituto Brasileiro de Geografia e Estatística. Accessed 16 June 23
- Johansen A (1996) A simple model of recurrent epidemics. *J Theor Biol* 178(1):45–51
- Kermack WO, McKendrick AG (1927) A contribution to the mathematical theory of epidemics. *R Soc Lond Proc Ser A* 115:700–721
- Kheiri H, Jafari M (2019) Stability analysis of a fractional order model for the HIV/AIDS epidemic in a patchy environment. *J Comput Appl Math* 346:323–339
- Klepac P, Megiddo I, Grenfell BT, Laxminarayan R (2016) Self-enforcing regional vaccination agreements. *J R Soc Interface* 13:1
- Kouokam E, Auger P, Hbid H, Tchuenta M (2008) Effect of the number of patches in a multi-patch SIRS model with fast migration on the basic reproduction rate. *Acta Biotheor* 56(1–2):75–86
- Leoneno V, Arzamashev S, Bobashev G (2020) Contact patterns and influenza outbreaks in Russian cities: a proof-of-concept study via agent-based modeling. *J Comput Sci* 44:101156
- Liu J, Bai Z, Zhang T (2018) A periodic two-patch SIS model with time delay and transport-related infection. *J Theor Biol* 437:36–44
- Ma S, Zhang J, Zeng M, Yun Q, Guo W, Zheng Y, Zhao S, Wang MH, Yang Z (2020) Epidemiological parameters of COVID-19: case series study. *J Med Internet Res* 22:10
- Medrek M, Pastuszak Z (2021) Numerical simulation of the novel coronavirus spreading. *Expert Syst Appl* 166:114109
- Monteiro LHA (2020) An epidemiological model for SARS-CoV-2. *Ecol Complex* 43:100836
- Monteiro LHA, Fanti V, Tessaro A (2020) On the spread of SARS-CoV-2 under quarantine: a study based on probabilistic cellular automaton. *Ecol Complex* 44:100879
- Moore C, Newman MEJ (2000) Epidemics and percolation in small-world networks. *Phys Rev E* 61(5):5678–5682
- Mpolya EA, Yashima K, Ohtsuki H, Sasaki A (2014) Epidemic dynamics of a vector-borne disease on a villages-and-city star network with commuters. *J Theor Biol* 343:120–126
- Nipa KF, Allen LJ (2020) Disease emergence in multi-patch stochastic epidemic models with demographic and seasonal variability. *Bull Math Biol* 82(12):1–30
- Notas técnicas da Fiocruz (2022) <https://bigdata-covid19.icict.fiocruz.br/>. Accessed 10 May 2
- Ogren P, Martin CF (2000) Optimal vaccination strategies for the control of epidemics in highly mobile populations. In: Proceedings of the 39th IEEE conference on decision and control (Cat. No.00CH37187), vol 2. pp 1782–1787
- Ogren P, Martin CF (2002) Vaccination strategies for epidemics in highly mobile populations. *Appl Math Comput* 127(2):261–276. [https://doi.org/10.1016/S0096-3003\(01\)00004-2](https://doi.org/10.1016/S0096-3003(01)00004-2)
- Prosper O, Ruktanonchai N, Martcheva M (2012) Assessing the role of spatial heterogeneity and human movement in malaria dynamics and control. *J Theor Biol* 303:1–14
- Ramos ABM, Schimit PHT (2019) Disease spreading on populations structured by groups. *Appl Math Comput* 353:265–273
- Rautureau S, Dufour B, Durand B (2010) Vulnerability of animal trade networks to the spread of infectious diseases: a methodological approach applied to evaluation and emergency control strategies in Cattle, France, 2005. *Transbound Emerg Dis* 58:110–120
- Rock K, Brand S, Moir J, Keeling MJ (2014) Dynamics of infectious diseases. Reports on progress in physics. *Phys Soc (Great Britain)* 77(2):026602
- Salmani M, van den Driessche P (2006) A model for disease transmission in a patchy environment. *Discrete Continuous Dyn Syst - B* 6(1):185–202. <https://doi.org/10.3934/dcdsb.2006.6.185>
- Sander LM, Warren CP, Sokolov I, Simon C, Koopman J (2002) Percolation on disordered networks as a model for epidemics. *Math Biosci* 180:293–305
- Schimit PHT, Monteiro LHA (2009) On the basic reproduction number and the topological properties of the contact network: an epidemiological study in mainly locally connected cellular automata. *Ecol Model* 220(7):1034–1042
- Schimit PHT, Pereira FH (2018) Disease spreading in complex networks: a numerical study with principal component analysis. *Expert Syst Appl* 97:41–50
- Senapati A, Sardar T, Ganguly KS, Ganguly KS, Chattopadhyay AK, Chattopadhyay J (2019) Impact of adult mosquito control on dengue prevalence in a multi-patch setting: a case study in Kolkata (2014–2015). *J Theor Biol* 478:139–152
- Singhal T (2020) A review of coronavirus disease-2019 (COVID-19). *Indian J Pediatr* 87(4):281–286. <https://doi.org/10.1007/s12098-020-03263-6>
- Sirakoulis GC, Karafyllidis I, Thanailakis A (2000) A cellular automaton model for the effects of population movement and vaccination on epidemic propagation. *Ecol Model* 133(3):209–223

- Tanne JH, Hayasaki E, Zastrow M, Pulla P, Smith P, Rada AG (2020) COVID-19: how doctors and healthcare systems are tackling coronavirus worldwide. *BMJ* 368(March):1–5
- Van Den Driessche P, Watmough J (2002) Reproduction numbers and sub-threshold endemic equilibria for compartmental models of disease transmission. *Math Biosci* 180(1–2):29–48
- van Ravensway J, Benbow ME, Tsonis AA, Pierce SJ, Campbell LP, Fyfe JAM, Hayman JA, Johnson PDR, Wallace JR, Qi J (2012) Climate and landscape factors associated with Buruli ulcer incidence in Victoria, Australia. *PLoS One* 7(12):e51074
- Verelst F, Kuylens E, Beutels P (2020) Indications for healthcare surge capacity in European countries facing an exponential increase in coronavirus disease (COVID-19) cases, March 2020. *Eurosurveillance* 25(13):1–4
- Wang W, Zhao XQ (2006) An epidemic model with population dispersal and infection period. *SIAM J Appl Math* 66(4):1454–1472
- Wang W, Zhao XQ (2008) Threshold dynamics for compartmental epidemic models in periodic environments. *J Dyn Differ Equ* 20(3):699–717
- Watts D, Strogatz S (1998) Collective dynamics of small-world networks. *Nature* 393:440–442
- Westgarth C, Gaskell RM, Pinchbeck GL, Bradshaw JWS, Dawson S, Christley RM (2009) Walking the dog: exploration of the contact networks between dogs in a community. *Epidemiol Infect* 137(8):1169–1178
- Wolfram S (1994) Cellular automata and complexity: collected papers. Westview Press, New York
- Wu JT, Leung K, Bushman M, Kishore N, Niehus R, de Salazar PM, Cowling BJ, Lipsitch M, Leung GM (2020) Estimating clinical severity of COVID-19 from the transmission dynamics in Wuhan, China. *Nat Med* 26:506–510
- Xi W, Pei T, Liu Q, Song C, Liu Y, Chen X, Ma J, Zhang Z (2020) Quantifying the time-lag effects of human mobility on the COVID-19 transmission: a multi-city study in China. *IEEE Access* 8:216752–216761
- Yakowitz S, Gani J, Hayes R (1990) Cellular automaton modeling of epidemics. *Appl Math Comput* 40:41–54
- Zakary O, Larrache A, Rachik M, Elmouki I (2016) Effect of awareness programs and travel-blocking operations in the control of HIV/AIDS outbreaks: a multi-domains SIR model. *Adv Differ Equ* 1:2016
- Zakary O, Rachik M, Elmouki I, Lazaiz S (2017) A multi-regions discrete-time epidemic model with a travel-blocking vicinity optimal control approach on patches. *Adv Differ Equ* 1:2017
- Zhao S, Bauch CT, He D (2018) Strategic decision making about travel during disease outbreaks: a game theoretical approach. *J R Soc Interface* 15:9
- Zhou T, Liu Q, Yang Z, Liao J, Yang K, Bai W, Lu X, Zhang W (2020) Preliminary prediction of the basic reproduction number of the Wuhan novel coronavirus 2019-ncov. *J Evid Based Med* 13(1):3–7

**Publisher's Note** Springer Nature remains neutral with regard to jurisdictional claims in published maps and institutional affiliations.

Springer Nature or its licensor (e.g. a society or other partner) holds exclusive rights to this article under a publishing agreement with the author(s) or other rightsholder(s); author self-archiving of the accepted manuscript version of this article is solely governed by the terms of such publishing agreement and applicable law.